Acta Cryst. (1996). B52, 406–413

A Synchrotron X-ray Study of the Electron Density in $SmFeO_3$

E. N. MASLEN,[a] V. A. STRELTSOV[a]* AND N. ISHIZAWA[b]

[a]*Crystallography Centre, University of Western Australia, Nedlands 6907, Australia, and* [b]*Research Laboratory of Engineering Materials, Tokyo Institute of Technology, 4259 Nagatsuta, Midori-Ku, Yokohama 227, Japan. E-mail: strel@crystal.uwa.edu.au*

(*Received 20 July 1995; accepted 11 December 1995*)

Abstract

Structure factors for small, hydrothermally grown samarium orthoferrite, $SmFeO_3$, were measured with focused $\lambda = 0.7$ Å synchrotron radiation. Approximate high symmetry in the $\Delta\rho$ images indicates that cations deform the electron density far more strongly than the O atoms. The most obvious effect is on distribution of the Fe atoms. The influence of the nearest low-symmetry (C_s) O coordination on the electron density of the Sm cation is weak by comparison with that of the Sm–Fe interactions, as is illustrated by the high symmetry of the $\Delta\rho$ map near the Sm atom. The Sm–Fe interactions appear to affect the magnetic ordering and spin configuration of the Fe atoms. Space group *Pnma*, orthorhombic, M_r = 254.20, a = 5.6001 (3), b = 7.7060 (7), c = 5.3995 (6) Å, V = 233.01 (4) Å^3, Z = 4, D_x = 7.246 Mg m^{-3}, $\mu_{0.7}$ = 28.5 mm^{-1}, $F(000)$ = 448, T = 293 K, R = 0.017, wR = 0.021, S = 3.83 (8) for 1329 unique reflections.

1. Introduction

Synchrotron electromagnetic radiation (SR) emitted by transversely accelerated relativistic electrons or positrons has become a very powerful tool for exploring basic properties of materials that previously were hardly accessible. High noise due to limited intensity, larger crystal specimens and, consequently, unreliable extinction corrections led to poor reproducibility in X-ray tube source experiments (*e.g.* Streltsov & Maslen, 1992). Property predictions were inaccurate. The high-accuracy deformation density ($\Delta\rho$) images measured with SR allows the reorganization of the electron density in the atoms that form crystalline solids to be depicted unambiguously, sometimes with surprising conclusions. Thus, SR diffraction $\Delta\rho$ images for yttrium orthoferrite, $YFeO_3$ (du Boulay, Maslen, Streltsov & Ishizawa, 1995) show that the metal–metal interactions in this compound influence the crystal structure and electron densities strongly, at distances beyond the range of normal chemical bonds. Such effects are subordinate to the nearest-neighbour cation–anion interactions in terms of energy, but influence the $\Delta\rho$ image strongly. Large cation–anion effects on $\Delta\rho$ are more probable when the rare earth (RE) atom site symmetry (C_s) is low.

The crystal structure of $SmFeO_3$, along with those of other rare earth orthoferrites, was first analysed from a classical crystal chemistry point of view by Marezio, Remeika & Dernier (1970). Although the $SmFeO_3$ structural parameters are close to those for $YFeO_3$, resembling the distorted perovskite structure of $CaTiO_3$, substitution of diamagnetic Y by paramagnetic Sm introduces complicated new terms into the Hamiltonian for the system, including those due to interactions between unlike magnetic atoms.

The pure antiferromagnetism of $SmFeO_3$ at room temperature is exceptional among the RE orthoferrites. The compound exhibits weak ferromagnetism only at elevated temperatures below T_N = 674 K. Over the temperature range 457–465 K there is a continuous second-order phase transition of the spin orientation in the *Pnma* *bc* plane. The crystal becomes pure antiferromagnetic (a Morin-type transition) at $T < 457$ K with spins arranged along the [001] direction. The magnetic substructure in $SmFeO_3$ is similar to that in $YFeO_3$, with two interpenetrating pseudo-cubic face-centred Fe sublattices in which each Fe cation is surrounded octahedrally by six antiferromagnetic Fe atoms as nearest neighbours.

The magnitudes of the ordered Fe moments of *ca.* 4.6 Bohr magnetons for several RE orthoferrites at saturation temperature, measured by Koehler, Wollan & Wilkinson (1960) using neutron diffraction, were significantly smaller than the expected 5.0 Bohr magnetons. Reduction of the magnetic moment on the Fe atoms, also observed in $YFeO_3$, was related by Tofield & Fender (1970) to covalency effects between magnetic ions and the ligands.

The isotropic Heisenberg Fe–Fe exchange interactions considerably exceed the RE–Fe exchange and determine the high T_N of the Fe sublattice. However, as proved by numerous studies (*e.g.* Belov, Zvezdin & Kadomtseva, 1987), the antisymmetric part of the anisotropic 'non-Heisenberg' (Dzyaloshinski–Moria) Fe–Fe exchange in combination with RE–Fe exchange plays an important role in the anisotropic properties of orthoferrites. At temperatures below T_N it makes a considerable contribution to the weak ferromagnetic moment and determines the mechanism of the spin-reorientation transition. RE-sublattice spins orient only at very low temperatures.

As the higher spin-reorientation temperature in $SmFeO_3$ suggests that the RE–Fe interactions influence the system more strongly, it is desirable to identify the mechanism for these interactions. It is usually considered that the electronic states of magnetic ions are well represented by localized atomic orbitals, for orthoferrites that are insulators. The exchange interactions are believed to originate in superexchange mechanisms that invoke O-atom *p*-orbitals as intermediates.

Analysis of $\Delta\rho$ maps, focusing on the influence of cation–cation interactions and of the crystal field on the density near the cations, should assist our understanding of these magnetic properties, first of $SmFeO_3$ itself and then by inference for the whole RE orthoferrite series.

2. Experimental

A synchrotron diffraction study by du Boulay *et al.* (1995) showed that the mosaic distributions for hydrothermally grown crystals of $YFeO_3$ were more uniform than those for flux grown crystals. Their uniformity allowed secondary extinction corrections for small samples to be determined reliably. Flux grown orthoferrites often exhibit multiple twinning, with large mosaics and consequently high extinction that is usually both anisotropic and non-uniform. To ascertain whether samples suitable for high-precision diffraction imaging could be prepared, $SmFeO_3$ crystals were also prepared hydrothermally following the recipe of du Boulay *et al.* (1995) for $YFeO_3$. The $SmFeO_3$ specimens were precipitated from a solution of Sm_2O_3 + Fe_2O_3 (0.2 wt %)–NaOH (53 wt %) in H_2O, in a sealed 2 ml Pt tube (fill factor *ca* 0.7), inserted in an autoclave for 2 d at 653 K. Small dark red $SmFeO_3$ crystals were removed after the tube was cut open. The crystal chosen for synchrotron X-ray diffraction measurements was bounded by two (010), two (101), two (10$\bar{1}$) and two (11$\bar{1}$) faces with distances 2 × 40, 2 × 14, 2 × 14, 6 and 19 μm, respectively, from the crystal centre. These dimensions were measured and faces indexed using optical and scanning electron Philips SEM505 microscopes. The major faces of the crystal are similar to those for $YFeO_3$ (du Boulay *et al.*, 1995) and correspond to the ideal pseudo-cubic perovskite crystal faces. This supports earlier observations that the crystal habit for RE aluminates and orthoferrites is influenced more strongly by the pseudo-cell than by the true crystallographic cell. The (11$\bar{1}$) face was deformed. This deformation was described by a (11$\bar{3}$) face spaced 5 μm from the crystal centre.

Diffraction intensities were measured with 0.7000 (2) Å synchrotron X-radiation using the BL14A four-circle diffractometer (Satow & Iitaka, 1989) at the Tsukuba Photon Factory. Vertically polarized SR from a vertical wiggler was monochromated by a double Si (111) crystal monochromator, and focussed using a curved mirror. The polarization ratio, *i.e.* the fraction of the total incident beam intensity with its electric vector vertical, is 0.95. An incident beam slit, 0.4 mm in diameter, installed before the monitor Ar gas-flow ion counter, and a collimator, 0.2 mm in diameter, placed after the monitor chamber, provide an intense and adequately homogeneous beam. By positioning the specimen slightly off-focus, changes in the SR intensity due to particle beam instabilities were minimized. Since the stored positron beam decays exponentially with time, an ion chamber was used to monitor the incident beam intensity. The alignment of the first monochromator crystal and of the vertical translations of the mirror were optimized automatically by flux maximization every 20 min during data collection. With this automatic optics optimization, the intensity of the incident beam is stable within 1% over a 1 day period. A 3 × 3 mm receiving slit was placed in front of the scintillation counter. The higher harmonics in the beam from the monochromator are removed by the paired discriminators.

Lattice constants were evaluated from the diffractometer angles for five pairs of Friedel-related reflections at 2θ values of 54.03 (0±10,0), 60.00 (±800), 62.47 (00±8) and 62.96° (6±80 and −6±80). Reflection intensities were measured systematically using $\omega/2\theta$ scans for a complete sphere of reciprocal space with $(\sin\theta/\lambda)_{max}$ = 1.094 Å^{-1}, $-12 \le h \le 12$, $-16 \le k \le 16$, $-11 \le l \le 11$. Intensities were corrected for deadtime counting losses using the polynomial expansion by Hester, Maslen, Spadaccini, Ishizawa & Satow (1993). The NaI counter deadtime was measured to be 1.2 μs. Strong synchrotron intensities with count rates higher than 50 000 cps were reduced by Au foil with the attenuation factor 17.62. Six standard reflection intensities were remeasured every 100 reflections to monitor incident beam stability.

No reflections were classified arbitrarily as 'unobserved'. Measured intensities were normalized using the incident beam intensities monitored during each scan. Integrated intensities were further modified and structure-factor variances from counting statistics were adjusted for source instability, as indicated by the standards (Rees, 1977). Variances consistent with Poisson statistics were retained. Those for the other reflections were increased according to the scatter of equivalents following a Fisher test. Further experimental details are set out in Table 1.*

Lorentz and polarization corrections were applied. Absorption correction factors (Alcock, 1974) were evaluated analytically using a linear absorption coefficient μ at 0.7 Å evaluated from atomic absorption coefficients calculated by Creagh (1992). The reference state for all structure-factor calculations was the independent atom model (IAM) evaluated using spherical atomic scattering

* A list of structure factors has been deposited with the IUCr (Reference: AS701). Copies may be obtained through The Managing Editor, International Union of Crystallography, 5 Abbey Square, Chester CH1 2HU, England.

Table 1. *Experimental and refinement data for $SmFeO_3$*

Radiation	Synchrotron
λ (Å)	0.7000 (2)
Diffractometer	PF†
Monochromator	Si(111)
Scan speed (° min^{-1})	16
Peak scan width $[a + b \tan\theta]$ (°)	1.0; 0.0
Maximum 2θ (°)	99.98
Max. intensity variation of standards (%)	±(800), ±(0,10,0), ±(008), 5.0
Reflections measured	9625
Transmission range, min.;max.	0.237; 0.612
Independent reflections	1329
Extinction,‡ r^*	$\|r^*\| < \sigma(r^*)$, no extinction applied
R_{int} (F^2)	
Before	0.074
After absorption	0.036
R	0.020
wR	0.023
S	4.23 (8)
Max. shift/e.s.d.	0.3×10^{-4}
$\Delta\rho$, min.; max. (e Å^{-3})	−4.1;+3.0
Extinction§ (refinement 1), r^*	0.105 (7) × 10^4
Min. extinction y¶ (hkl)	0.83, (002)
R	0.017
wR	0.020
S	3.71 (7)
Max. shift/e.s.d.	0.9×10^{-4}
$\Delta\rho$, min.; max. (e Å^{-3})	−2.41; +3.1
Extinction§ (refinement 2), r^*	0.055 (5) × 10^4
Min. extinction y¶ (hkl)	0.89, (002)
R	0.017
wR	0.021
S	3.83 (8)
Max. shift/e.s.d.	0.9×10^{-4}
$\Delta\rho$, min.; max. (e Å^{-3})	−3.0; +3.1
$\sigma(\Delta\rho)$** (e Å^{-3})	0.25

† The BL14A four-circle diffractometer (Satow & Iitaka, 1989) at the Tsukuba Photon Factory, Japan. ‡ As proposed by Maslen & Spadaccini (1993). § Zachariasen (1967) extinction corrections included in least-squares structure refinement (Larson, 1970). ¶ $F_{obs} = yF_{kin}$, where F_{kin} is the value of the kinematic structure factor. ** Mean e.s.d. value (Cruickshank, 1949).

factors from *International Tables for X-ray Crystallography* (1974, Vol. IV) with dispersion corrections $\Delta f'$, $\Delta f''$ of −0.177, 3.365 for Sm, 0.343, 0.826 for Fe, and 0.011, 0.006 for O at $\lambda = 0.7$ Å calculated by Creagh (1992). All subsequent calculations utilized the *Xtal*3.2 system of crystallographic programs (Hall, Flack & Stewart, 1992) implemented on Sun SPARC and DEC 5000/120 work stations.

Extinction corrections were estimated following the procedures used in the $YFeO_3$ study (du Boulay *et al.*, 1995). Before refining structural parameters, extinction correction for the full data set based on intensities for symmetry-equivalent reflections with different path lengths (Maslen & Spadaccini, 1993) was attempted. Being an unbiased estimator of structure-factor precision, this algorithm potentially checks the more precise values that minimize differences between observed and calculated structure factors. The extinction parameter determined with different subsets of strong reflections varied from slightly negative to positive by amounts less than the e.s.d.s. Although no extinction correction was applied at this stage, the e.s.d.s range allowed a y_{min} (F) extinction correction of 0.89 to be estimated.

More precise though potentially biased extinction corrections were evaluated by refining an extinction parameter as part of least-squares optimization of the structural model. The widely invoked formula of Zachariasen (1967) was included in refinement 1 following the implementation of Larson (1970), yielding an extinction parameter (listed in Table 1) which indicates that extinction is significant. Refinement of the extinction corrections altered the scale factor and the $\Delta\rho$ density appreciably, as indicated by the min, max values in Table 1. The atomic charges calculated from the $\Delta\rho$ map for the Fe and O2 atoms by Hirshfeld (1977) partitioning for that refinement are almost neutral, as shown below. The more mild corrections indicated by comparison of equivalent reflections suggests that the extinction parameter determined as part of the structure refinement overcorrects the structure factors. To reduce dominance of the refinement by strong low-angle reflections with least-squares residuals $|F_o - F_c|/\sigma$ ranging up to 39, the scale factor was first optimized along with the structural parameters, but excluding extinction for a subset of 1309 reflections with $\sin\theta/\lambda > 0.26$ Å^{-1}, using unit weights. With the scale factor fixed, the extinction parameter for refinement 2 in Table 1 was determined along with structural atomic parameters using weights w equal to $1/\sigma^2(F_o)$. The extinction parameter thus determined was within 1 e.s.d. of the value estimated from intensities of the symmetry-related reflections. Thus, the extinction correction determined by least-squares refinement of the extinction parameter and scale factor separately is within the range of the estimates by the Maslen & Spadaccini (1993) algorithm.

With extinction fixed the scale factor varied only within 1 e.s.d. when refined along with 27 independent structural parameters, including all anisotropic vibration tensor elements, using the complete data set. These parameters were refined by full-matrix least-squares based on $|F|$ with $w = 1/\sigma^2(F_o)$ for all measured structure factors. The atomic charges in column 3 of Table 4 and the $\Delta\rho$ maps were calculated subsequently using the parameters from this refinement.

3. Structural parameters

The orthorhombic perovskite-like $SmFeO_3$ structure is depicted in Fig. 1. The refined positional and vibrational parameters are listed in Table 2, with selected bond lengths and Fe octahedral angles in Table 3. The cell dimensions and the atomic positions from Table 2 are within two and three decimal places, respectively, of those reported for $SmFeO_3$ by Marezio *et al.* (1970). Detailed characteristics of the structural geometries of the RE orthoferrites including $SmFeO_3$ were fully

Table 2. *Fractional coordinates and anisotropic vibration parameters ($U_{ij} \times 10^5$,Å^2) with e.s.d.'s in parentheses for $SmFeO_3$*

$$T = \exp[-2\pi^2(U_{11}(ha^*)^2 + \ldots + 2U_{12}ha^*kb^* + \ldots)].$$

	x	y	z	U_{11}	U_{22}	U_{33}	U_{12}	U_{13}	U_{23}
Fe	0	0	1/2	446 (8)	413 (6)	513 (7)	34 (8)	11 (5)	−9 (5)
Sm	0.05728 (2)	1/4	−0.01335 (2)	520 (3)	546 (2)	635 (3)	0	−77 (2)	0
O1	0.4707 (2)	1/4	0.0953 (3)	840 (40)	427 (32)	808 (40)	0	−118 (33)	0
O2	−0.2991 (2)	−0.0498 (1)	0.3007 (2)	568 (26)	795 (27)	697 (27)	−100 (20)	−160 (21)	87 (21)

described by Marezio *et al.* (1970). Selected interatomic distances and angles from Table 3 closely resemble the values presented by these authors.

The main distortions from the ideal cubic perovskite structure are those within the RE—O bonding polyhedra that stabilize the orthorhombic structure. The FeO_6 coordination remains almost ideally octahedral throughout the whole orthoferrite series. The three Fe—O distances range from 2.0008 (4) to 2.0276 (9) Å and resemble those for $YFeO_3$ (du Boulay *et al.*, 1995) as closely as expected from the standard deviations. The average Fe—O and O—O distances of 2.0135 (8) and 2.848 (2) Å, respectively, evaluated for the FeO_6 octahedron from Table 2 hardly vary throughout all the orthoferrites with RE from Pr to Lu (Marezio *et al.*, 1970), including $YFeO_3$ (du Boulay *et al.*, 1995).

The Fe—O—Fe angles relevant to magnetic superexchange are included in Table 3. Buckling of the corner-shared octahedra (Fig. 1) changes the Fe—O—Fe angles from the ideal value of 180°.

The mean RE—O distance varies slightly across the whole series, as shown by Marezio *et al.* (1970). The ideal REO_{12} polyhedron with equal RE—O distances

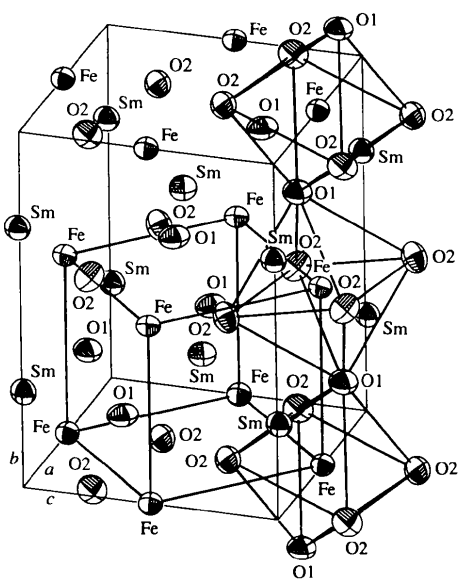

Fig. 1. Orthorhombic unit cell for $SmFeO_3$ with vibrational ellipsoids at the 99% probability level.

Table 3. *Selected interatomic distances (Å) and angles (°) for $SmFeO_3$*

Sm—Sm^{i}	(2)	3.7909 (3)	Fe—Fe^{viii}	(2)	3.8530 (3)
Sm—Sm^{ii}	(2)	3.9087 (3)	Fe—Fe^{vii}	(4)	3.8896 (2)
Sm—Sm^{iii}	(2)	3.9910 (3)	Fe—O1^{v}	(2)	2.0008 (4)
Sm—Fe^{iii}	(2)	3.1406 (2)	Fe—O2^{ix}	(2)	2.012 (1)
Sm—Fe^{iv}	(2)	3.2740 (3)	Fe—O2	(2)	2.0276 (9)
Sm—Fe	(2)	3.3908 (3)	O1—O1^{v}	(2)	3.260 (2)
Sm—Fe^{v}	(2)	3.6682 (2)	O1—O2^{ii}	(2)	2.806 (2)*
Sm—O1^{v}		2.309 (1)	O1—O2^{iii}	(2)	2.817 (1)*
Sm—O1		2.388 (1)	O1—O2^{x}	(2)	2.869 (1)*
Sm—O1^{i}		3.180 (1)	O1—O2^{xi}	(2)	2.880 (2)*
Sm—O1^{vi}		3.337 (1)	O1—O2^{xii}	(2)	2.733 (2)
Sm—O2^{vii}	(2)	2.3403 (9)	O2—O2^{xiii}	(2)	2.853 (1)*
Sm—O2^{ii}	(2)	2.573 (1)	O2—O2^{vii}	(2)	2.860 (2)*
Sm—O2^{iii}	(2)	2.7026 (9)	O2—O2^{xiv}		3.085 (1)
Sm—O2	(2)	3.493 (1)	O2—O2^{xv}		3.207 (1)

Iron octahedra angles

O1^{v}—Fe—O2	88.75 (5)	O1^{v}—Fe—Fe^{xvi}	180 by symmetry
O1^{v}—Fe—O2^{ix}	88.74 (5)	O2^{xiii}—Fe—O2^{ix}	
O2^{xiii}—Fe—O2^{xii}	90.14 (4)	Fe^{iii}—O1—Fe^{xi}	148.67 (8)
		Fe—O2—Fe^{vii}	148.64 (5)

Symmetry codes: (i) $x-\frac{1}{2}, \frac{1}{2}-y, -\frac{1}{2}-z$; (ii) $-x, \frac{1}{2}+y, -z$; (iii) $\frac{1}{2}+x, \frac{1}{2}-y, \frac{1}{2}-z$; (iv) $x, y, z-1$; (v) $x-\frac{1}{2}, \frac{1}{2}-y, \frac{1}{2}-z$; (vi) $x-1, y, z$; (vii) $-x-\frac{1}{2}, -y, z-\frac{1}{2}$; (viii) $-x, \frac{1}{2}+y, 1-z$; (ix) $-\frac{1}{2}-x, -y, \frac{1}{2}+z$; (x) $1+x, y, z$; (xi) $\frac{1}{2}-x, -y, z-\frac{1}{2}$; (xii) $-x, -y, 1-z$; (xiii) $\frac{1}{2}+x, y, \frac{1}{2}-z$; (xiv) $x, -\frac{1}{2}-y, z$; (xv) $-1-x, -y, 1-z$; (xvi) $\frac{1}{2}-x, -y, \frac{1}{2}+z$.

* O—O distances in the FeO_6 octahedra.

becomes distorted to such a degree that it is possible to distinguish six or eight or more nearest-neighbour O atoms from among the 12 in the ideal structure. Average values for the first six RE—O distances for $YFeO_3$ reported by du Boulay *et al.* (1995) and for $SmFeO_3$ from Table 3 are 2.344 and 2.421 Å, respectively. The averages of the first eight are 2.427 and 2.491 Å; those for the other four are 3.446 and 3.376 Å. The significant difference between the means of the eight shortest and the four longest M—O distances in $YFeO_3$ and $SmFeO_3$ of 1.019 and 0.885 Å, respectively, may be interpreted following Marezio *et al.* (1970) as indicating that the coordination of the RE cations is close to eightfold. The slightly larger difference between the first six nearest and the next six O atoms in $YFeO_3$ compared with $SmFeO_3$ may indicate in turn its dependency on the Y coordination number reduction in $YFeO_3$. The optimum coordination number depends on the size of the RE

cation. The Sm cations are larger than Y cations and the $SmFeO_3$ structure is less distorted than that of $YFeO_3$. However, the ionic radius for the RE atom in RE orthoferrites is not a well defined concept, since its value can be varied depending on the recipe by which one chooses the coordination number. It is certainly clear that the effective shape of the RE atom in these structures is anisotropic, to a degree that anisotropy increases as the mean radius of the RE atom decreases.

This change of the distortions of the RE coordination in Y and Sm orthoferrites does not alter the local symmetry (C_s) of the crystal field at the central RE atom. It should have only a second-order effect on the electron density near the RE cation. However, the distances between atoms of the RE polyhedra may affect the atomic vibration parameters.

4. Vibration parameters

Vibration ellipsoids for $SmFeO_3$ at the 99% probability level are depicted in Fig. 1. Vibration amplitudes for all atoms in Table 2 are systematically higher than those for $YFeO_3$ (du Boulay *et al.*, 1995), suggesting that the $SmFeO_3$ structure is packed less tightly. The vibration parameters for $SmFeO_3$ by Marezio *et al.* (1970), although significantly larger than those in Table 2, show the same trend $U_{33} > U_{11} > U_{22}$ for Fe, $U_{33} > U_{22} > U_{11}$ for Sm, $U_{11} > U_{33} > U_{22}$ for O1 and $U_{22} > U_{33} > U_{11}$ for O2. Both O-atom vibrations are significantly anisotropic, as shown in Table 2. The U_{22} mean-square amplitudes in $YFeO_3$ were also observed to reduce and increase for O1 and O2, respectively, by du Boulay *et al.* (1995). The short Fe—O1—Fe interaction parallel to the *b* axis (Fig. 1) reduces the O1-atom vibration markedly in the [010] direction, whereas the shorter Fe—O2—Fe interaction, approximately perpendicular to the *b* axis, reduces the O2-atom vibrations in both the [100] and [001] directions.

The vibration ellipsoids for the O atoms at the intermediate RE—O distances of 2.573 (1) and 2.7026 (9) Å in $SmFeO_3$, and of 2.496 (1) and 2.675 (1) Å in $YFeO_3$ (du Boulay *et al.*, 1995) tend to have the largest amplitude directed approximately along the RE—O bond, suggesting that these O atoms may occupy alternative sites either statically or moving between them dynamically.

The vibration parameters in Table 2 for the Fe atom are significantly less than those for Sm and the O atoms, as expected from rigidity of the FeO_6 octahedron. The anisotropy of vibrations for the cations differ from that observed for $YFeO_3$. More pronounced vibrations in the [001] direction for $SmFeO_3$ replace the slight predominance of vibrations in the [010] direction for $YFeO_3$. The strong increase of the *c* parameter compared with *a* and *b* on going from $YFeO_3$ to $SmFeO_3$ confirms this trend. Y atoms with their smaller radii move further from the *b* axis in the (010) plane and vibrate more strongly along the [010] direction. The $SmFeO_3$ structure is packed tightly along the —O1—Fe—O1—Fe— line in the *b* direction and less tightly along the *c* axis.

Table 4. *Atomic charges in electrons from the Hirshfeld partitioning of $\Delta\rho$ for $SmFeO_3$*

	No extinction applied	Extinction refinement 1	Extinction refinement 2
Sm	2.2 (1)	0.6 (1)	1.1 (1)
Fe	1.9 (1)	0.1 (1)	0.9 (1)
O1	−1.40 (8)	−0.58 (8)	−0.92 (8)
O2	−1.25 (8)	−0.06 (8)	−0.54 (8)

5. Atomic charges

The atomic charges in Table 4 were determined for each different refinement in Table 1 by projecting $\Delta\rho$ onto atomic density basis functions (Hirshfeld, 1977). The variation of the charge for the same atom with the refinement procedure mainly reflects their dependence on the extinction corrections, as discussed in recent SR studies of metal oxides: the orthoferrite $YFeO_3$ (du Boulay *et al.*, 1995) and the C-type Y_2O_3, Dy_2O_3 and Ho_2O_3 sesquioxides (Maslen, Streltsov & Ishizawa, 1996). Extinction has its strongest effect on the low-angle reflections to which the charges are most sensitive. The sensitivity of atomic charge to extinction increases with atomic number. Overestimated extinction correction tends to reduce polarity determined for ionic crystals by spuriously increasing the electron count on the heavier cations. The charges for refinement 2 are believed to be more reliable, and their signs, being consistent with electronegativities for all the atoms, suggest electron transfer from Sm and Fe cations towards the O anions. The atomic charges in $SmFeO_3$ and $YFeO_3$ (du Boulay *et al.*, 1995) are concordant, and in particular, the charges of oxygens in both crystals agree within the e.s.d.s.

6. Electron density

Deformation density sections in the (010) and $(\frac{1}{2}00)$ planes through the Fe atoms, and in the plane through the FeO_4 unit containing the Fe–O1 and the longer Fe–O2 vectors, similar to those for $YFeO_3$ presented by du Boulay *et al.* (1995), are shown in Figs. 2, 3 and 4(*a*), respectively. Fig. 4(*b*) displays the section in the plane through the FeO_4 unit containing the Fe–O1 and the shorter Fe–O2 vectors. All maps are based on refinement 2 described in Table 1. The 0.5 e $Å^{-3}$ contour intervals are twice the $\sigma(\Delta\rho)$ value listed in Table 1.

The $\Delta\rho$ map in Fig. 2 is remarkable for the *mmm* symmetry that is closely approximated by the electron distribution in this plane, resembling the $\Delta\rho$ topol-

ogy in the corresponding $\Delta\rho$ section for $YFeO_3$. This approximate symmetry is higher than the inversion centre expected from the exact structural geometry around the Fe atom. It matches the *mmm* symmetry of the nearest-neighbour Fe cations with the shorter Fe–Fe vector along [001] more closely, in stark contrast to the lower symmetry of the O-atom positions projected in Fig. 2. However, the $\Delta\rho$ density symmetry is lower than the fourfold expected by considering interactions between the Fe cations in their ideal positions alone. The aspherical $\Delta\rho$ density accumulation near the Fe atoms is directed away from the near-neighbour O anions in a manner typical of the 3*d*-electron density for transition metals. However, it has only two pronounced positive $\Delta\rho$ density lobes in the [001] direction across the map, compared with approximate fourfold positive $\Delta\rho$ density near the Fe atoms in $YFeO_3$, which has diamagnetic Y cations. The polarization of the Fe-atom positive $\Delta\rho$ density in Fig. 2 relates to the spin polarization in the [001] direction. The reduced symmetry may thus be attributed to the perturbing effect of the magnetic Sm cations, rather than the neighbouring O anions. The Sm atoms projected in the Fig. 2 plane are located away from the central Fe atom at 3.1406 (2) and 3.6682 (2) Å in the [100] direction down the map, and at 3.2740 (3) and 3.3908 (3) Å in the [001] direction across the map. The Fe–Sm vectors differ significantly in length and the $\Delta\rho$ symmetry is affected by that length difference.

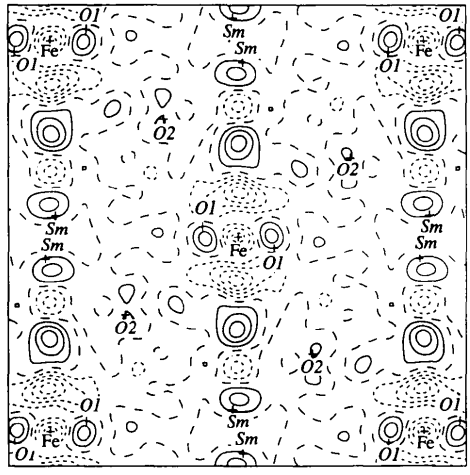

Fig. 2. $\Delta\rho$ for $SmFeO_3$ in the (010) plane through Fe atoms. Atoms deviating from the plane by ±1.93 (Sm and O1) and ±0.38 Å (O2) are shown in italics. Map borders 6.6 × 6.6 Å. Contour interval 0.5 e Å^{-3}, positive contours solid, negative contours short dashes.

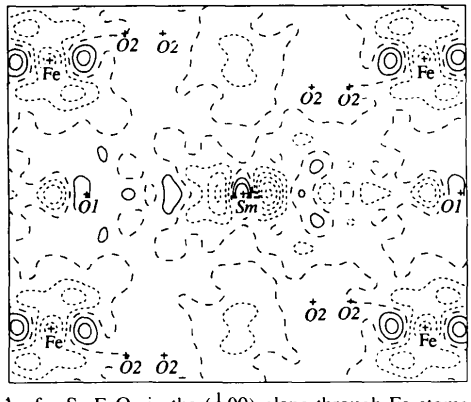

Fig. 3. $\Delta\rho$ for $SmFeO_3$ in the $(\frac{1}{2}00)$ plane through Fe atoms. Atoms deviating from the plane by −0.32 (Sm), 0.16 (O1) and ±1.12 and ±1.68 Å (O2) are shown in italics. Map borders 6.6 × 5.4 Å. Contours as for Fig. 2.

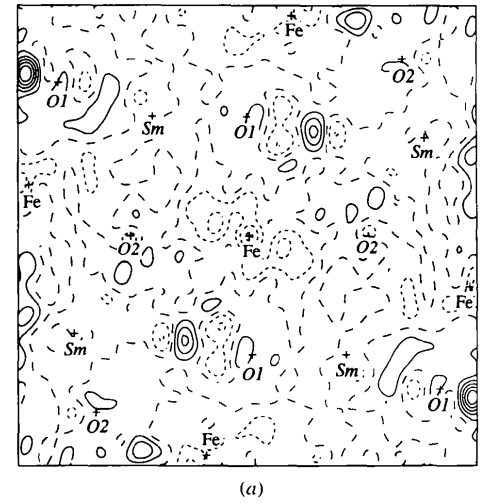

(*a*)

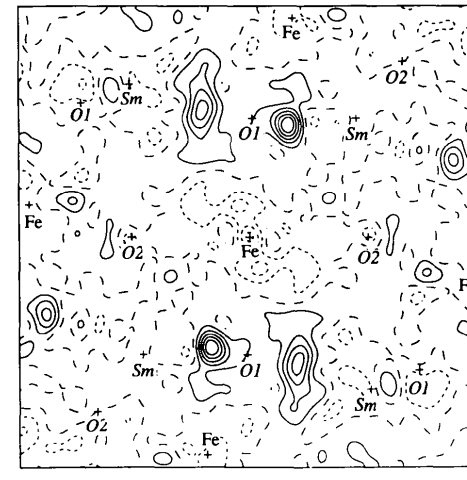

(*b*)

Fig. 4. $\Delta\rho$ for $SmFeO_3$ in the plane through Fe, O1 and O2 atoms with (*a*) the longer Fe—O2 contacts and (*b*) the shorter Fe—O2 contacts. Atoms deviating from the *a* plane by ±1.36 and ±1.77 (Sm), ±0.62 and ±0.65 (Fe), ±0.21 (O1), and ±0.52 Å (O2), and from the *b* plane by ±0.78 and ±1.61 (Sm), ±0.81 and ±0.90 (Fe), ±1.44 (O1), and ±0.65 Å (O2) are shown in italics. Map borders 7.8 × 7.8 Å. Contours as for Fig. 2.

Positive $\Delta\rho$ density accumulates near the nucleus of the Fe atom, whereas the depleted regions are further away. That topography suggests that the inner *d* subshells for the Fe atom are occupied, as is consistent with a low-spin $3d$-electron configuration for the Fe atom.

The $(\frac{1}{2}00)$ section through the Fe atoms in the plane of antiferromagnetically ordered spins parallel to the [001] direction is shown in Fig. 3, with the [001] direction across the map. The central Sm atom is -0.32 Å below this plane. The section shows an approximate local mirror in the $\Delta\rho$ density near the Sm atom, additional and perpendicular to the true crystallographic mirror plane at the Sm site. This higher than expected local symmetry again matches the geometrical disposition of the Fe atoms, ignoring that of the projected O atoms. The $\Delta\rho$ density near the Sm atom is dissimilar to that observed near the Y atom in the earlier study of $YFeO_3$. The room-temperature Fe magnetic moments in $YFeO_3$ are antiferromagnetically arranged only approximately along the [001] direction resulting in weak ferromagnetism parallel to the [010] axis. The $(00\frac{1}{2})$ section through the Fe atoms in $SmFeO_3$ (not shown) orthogonal to the [001] direction of spin arrangement reflects the crystallographic mirror plane symmetry similar to this section in $YFeO_3$. The influence of the low-symmetry (C_s) nearest-neighbour O coordination on the electron density of the Sm cation is weak by comparison to that due to Sm–Fe interactions in the *bc* plane, which appears to affect the magnetic ordering and spin configuration of the Fe atoms.

The $\Delta\rho$ densities near the O atoms is depicted in Figs. 3 and 4. The $\Delta\rho$ densities near the O2 atoms are depleted in both sections of Figs. 4(*a*) and (*b*). The $\Delta\rho$ features around the O2 atoms which have longer bonds to the cations are more diffuse. In contrast, the density is more localized around the O1 atom, reflecting the tighter O1 contacts with Fe and Sm atoms (Table 3). However, the excess $\Delta\rho$ density near O1 in Fig. 3 does not concentrate near a line bisecting the Fe—O1—Fe angle, as in $YFeO_3$, but is localized near the O nucleus and polarized toward the Fe and Sm atoms in Figs. 4(*a*) and (*b*). The large positive $\Delta\rho$ peaks around the O1 atoms in Figs. 4(*a*) and (*b*) are located in the crystallographic mirror plane through the Sm and O1 atoms. This is consistent with the basic requirements for covalent contributions to Fe—O—Fe and Sm—O—Fe superexchange interactions.

7. Concluding remarks

The accurate synchrotron $\Delta\rho$ images indicate that electron density in $SmFeO_3$ is perturbed significantly by non-bonded metal–metal interactions – a theme that continues through all recent SR studies of metal oxides: α-Al_2O_3 (Maslen, Streltsov, Streltsova, Ishizawa & Satow, 1993) and α-Fe_2O_3 (Maslen, Streltsov, Streltsova & Ishizawa, 1994), $YFeO_3$ orthoferrite (du Boulay *et al.*, 1995) and the C-type sesquioxides: Y_2O_3, Dy_2O_3 and Ho_2O_3 (Maslen *et al.*, 1996). The electron densities of cations are deformed more strongly by interaction with other cations than with O atoms, except where the O-coordination crystal field of the cation includes a low-symmetry component.

The topography of SR images indicates that valence electron density overlapping with closed inner subshells of cations is repelled by exchange towards regions of lower electrostatic potential more remote from the nuclei. The transferred density retains the symmetry of cation array. That is consistent with the observed regularity of cation arrays – which often exceeds that of the anions (O'Keeffe & Hyde, 1985).

In orthoferrites the most obvious effect of the cation–cation interactions on the $\Delta\rho$ symmetry is on distribution of the magnetic Fe atoms. The striking difference between $\Delta\rho$ densities around RE atoms in geometrically similar Sm and Y orthoferrite structures can be attributed to strong magnetic interactions between the Sm and Fe sublattices. Although being well beyond normal bond lengths, the Sm–Fe interactions strongly affect the magnetic phase transitions in $SmFeO_3$.

Since the 'overlap' or interference between the cation wavefunctions seems to be more significant and the O anion *p*-orbitals are relatively unimportant, the exchange mechanism responsible for magnetic properties of orthoferrites should include new terms that modify the cation-localized orbital model of indirect (super-) exchange interactions.

A low-spin configuration for the Fe atoms is indicated by the $\Delta\rho$ maps. This correlates with smaller magnetic moments of the Fe atoms in some RE orthoferrites observed by polarized neutron diffraction and complements the description of the phenomenon there by covalency and polarization effects on the spin density.

X-ray diffraction studies indicate that the RE coordination polyhedra in orthoferrites, the most distorted motif in the structure, exhibit either dynamic or static distortions that originate in fundamental bonding characteristics of the RE cations. Time-averaged pictures provided by diffraction images do not give all the information necessary to elucidate the nature of bonding in these structures, *i.e.* whether the intermediate length bonds are due to averaging of distances that are either long (non-bonded) or short (bonded). This requires additional, complementary information. When this hypothesis was proposed for similar systems near the active centres of metallo-proteins, it was supported strongly by EXAFS measurements.

This work was supported by the Australian Research Council. Financial support from the Australian National Beamline Facility (ANBF) is also acknowledged. The ANBF is funded by a consortium comprising the ARC, DITARD, ANSTO, CSIRO, ANU and UNSW. We are

indebted to Mr A. B. Fletcher (CSIRO) for assistance in growing crystals by hydrothermal methods.

References

Alcock, N. W. (1974). *Acta Cryst.* A**30**, 332–335.
Belov, K. P., Zvezdin, A. K. & Kadomtseva, A. M. (1987). *Sov. Sci. Rev. A Phys.* **9**, 117–222.
Boulay, D. du, Maslen, E. N., Streltsov, V. A. & Ishizawa, N. (1995). *Acta Cryst.* B**51**, 921–929.
Creagh, D. C. (1992). Private communication.
Cruickshank, D. W. (1949). *Acta Cryst.* **2**, 65–82.
Hall, S. R., Flack, H. D. & Stewart, J. M. (1992). *Xtal*3.2 *Reference Manual*. Universities of Western Australia, Australia, and Maryland, USA.
Hester, J. R., Maslen, E. N., Spadaccini, N., Ishizawa, N. & Satow, Y. (1993). *Acta Cryst.* B**49**, 967–973.
Hirshfeld, F. L. (1977). *Isr. J. Chem.* **16**, 198–201.
Koehler, W. C., Wollan, E. O. & Wilkinson, M. K. (1960). *Phys. Rev.* **118**, 58–70.
Larson, A. C. (1970). *Crystallographic Computing*, edited by F. R. Ahmed. Copenhagen: Munksgaard.
Marezio, M., Remeika, J. P. & Dernier, P. D. (1970). *Acta Cryst.* B**26**, 2008–2022.
Maslen, E. N. & Spadaccini, N. (1993). *Acta Cryst.* A**49**, 661–667.
Maslen, E. N., Streltsov, V. A. & Ishizawa, N. (1996). *Acta Cryst.* B**52**, 414–422.
Maslen, E. N., Streltsov, V. A., Streltsova, N. R. & Ishizawa, N. (1994). *Acta Cryst.* B**50**, 435–441.
Maslen, E. N., Streltsov, V. A., Streltsova, N. R., Ishizawa, N. & Satow, Y. (1993). *Acta Cryst.* B**49**, 973–980.
O'Keeffe, M. & Hyde, B. G. (1985). *An Alternative Approach to Non-molecular Crystals Structures With Emphasis on the Arrangements of Cations. Structure and Bonding*, Vol. 61, pp. 77–144. Berlin: Springer-Verlag.
Rees, B. (1977). *Isr. J. Chem.* **16**, 180–186.
Satow, Y. & Iitaka, Y. (1989). *Rev. Sci. Instrum.* **60**, 2390–2393.
Streltsov, V. A. & Maslen, E. N. (1992). *Acta Cryst.* B**48**, 651–653.
Tofield, B. C. & Fender, B. E. F. (1970). *J. Phys. Chem. Solids*, **31**, 2741–2749.
Zachariasen, W. H. (1967). *Acta Cryst.* A**23**, 558–564.